RESEARCH PAPER

Effects of evaporation-determined model of arc-cathode coupling on weld pool formation in GMAW process simulation

O. Mokrov[1] • M. Simon[1] • R. Sharma[1] • U. Reisgen[1]

Abstract

Currently used approaches for modeling the cathodic heat input in gas metal arc welding (GMAW) process simulation are usually based on very simplified approaches, either using a Rykalin-Rosenthal-distributed heat flux or a thermal conductivity approach, which do not reflect the deep physical processes involved. In this paper, a new approach for the calculation of the arc-cathode coupling in GMAW is presented, and the influence of the parameter variation on the formation of the weld pool is studied. The evaporation-determined model for arc-cathode coupling (EDACC) takes into account the recent findings on the plasma temperature in the GMAW arc, which is dominated by metal vapor, as well as the metal evaporation, which is readily ionized in the cathode region. It determines a relationship between the weld pool surface temperature and the heat flux as well as the current density distribution. As a result, the heat flux as well as the current density distribution is not axisymmetric. In this work, the model was coupled to a simplified weld pool simulation, and the influence of the model parameters like distribution of plasma temperature and welding velocity were investigated. Additionally, also the influence of the droplets on the weld pool surface temperature distribution and its effect on the arc-cathode attachment, as determined by the model, were studied.

1 Introduction

The gas metal arc welding (GMAW) process is widely used in the industry. However, due to the highly dynamic and non-linear behavior of the phenomena involved, the understanding of the physics behind the process is still not fully developed. Therefore, in the simulation of the process, substitution models are being used, which do not capture the full depth of the phenomena and their interactions. Only recently, a model for the cathode boundary layer has been published which can explain the distributions of heat flux and current density in GMAW on a physical basis [1]. In the present work, a study is presented which shows the effect of the new model on the formation of the weld pool and compares it with the effects of the currently widely used Rykalin-Rosenthal (Gaussian-shaped) surface heat source distribution [2].

2 Problem statement

In GMAW process simulation, the realization of the coupling between arc and weld pool is of essential importance for the fluid flow dynamic, which is mainly driven by droplet impact and electromagnetic Lorentz force. However, current approaches usually rely on simplified assumptions like a Rykalin-Rosenthal distribution of heat flux and current density, e.g., [3, 4], or by introducing a heat conduction coefficient between the arc and the weld pool as is realized in [5]. The approach using the Rykalin-Rosenthal distribution is based on the assumption that the processes responsible for the attachment are of statistical nature and therefore normally distributed. However, this approach has several drawbacks; as in general, in this approach, the highest heat flux will be localized at the position of the highest temperature, therefore leading to massive overheating and, when considering a realistic model for evaporation, like [6], also to considerable heat losses in this area

---

✉ M. Simon
  simon@isf.rwth-aachen.de

[1] ISF – Welding and Joining Institute, RWTH Aachen University, Pontstr. 49, 52062 Aachen, Germany

of high local overheating. Additionally, the experimental observations do not confirm boiling of the weld pool surface [7].

The second approach, of setting a heat conduction coefficient between the arc and the weld pool, as is realized in [5], seems arbitrary.

The model for the evaporation-determined arc-cathode coupling (EDACC) to the weld pool as presented in [1] aims at a more physically in-depth description of the processes. It is based on the theoretical modeling work on the cathode boundary layer by Benilov and others, e.g., [8–10]. It assumes that iron atoms are ionized in the cathode area, considering a plasma in local thermodynamic equilibrium (LTE) which has a temperature, that is a mixture of the temperature of the plasma bulk with the temperature of the evaporated iron atoms. Thereby, it determines the heat flux and the current density of the arc to the weld pool in dependence on the weld pool surface temperature as well as the adjacent plasma temperature. However, as the plasma itself is not self-consistently modeled in this case, the system cannot be regarded as fully closed. It also features the findings of [11–14] where it is shown that the iron vapor in the GMAW arc decreases the plasma temperatures to values down to 8000–9000 K in the center, when pure Argon is used as a shielding gas. This consideration is necessary in order to assure the most significant heating at surface temperatures much lower than the boiling temperature ($T_{boiling, steel} = 3144$ K) as seen in Fig. 1. Figure 2 shows the dependence of the current density according to the same model. Using these dependencies, it is possible to model a cathodic attachment by finding the distributions for heat flux and current density on the weld pool surface.

Additionally, since the attachment depends on the weld pool surface temperature, the influence by the droplets on the weld pool surface temperature also has a strong effect on the cathodic attachment, as was discussed in [1], as well.
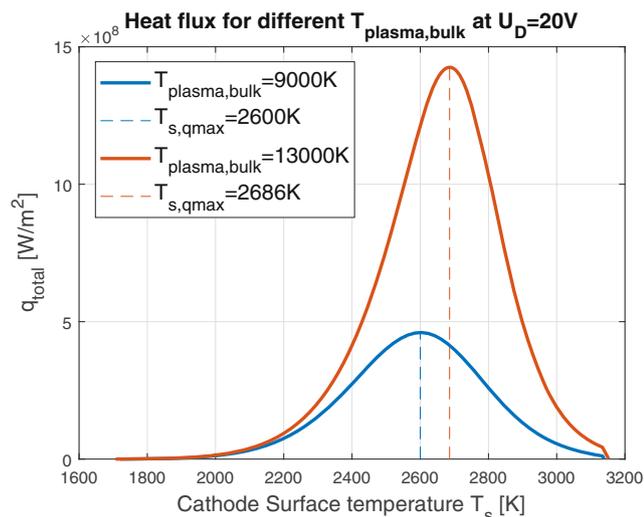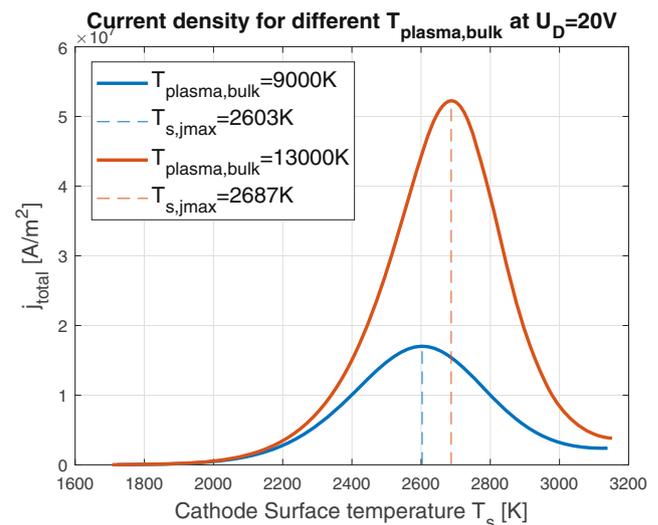

Fig. 2 Dependence of current density according to model [1] on surface temperature

The present work investigates the effects of the EDACC model according to [1] on the weld pool formation as well as the dependencies of the arc-cathode attachment on several welding parameters.

3 Model of the weld pool

The weld pool was modeled in Ansys CFX. For the calculation of the weld pool geometry, an approach without the consideration of a free surface was chosen due to consideration of the calculation speed. The mesh and the computational domain are depicted in Fig. 3. The domain is filled with steel, which is modeled as a liquid, moving through the domain, with a very high viscosity ν of 20 Pa s when the material

Fig. 1 Dependence of heat flux according to model [1] on surface temperature

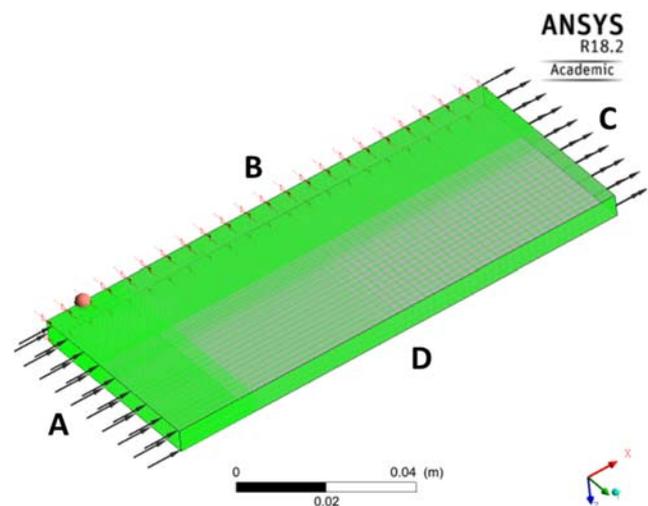Fig. 3 Mesh for weld pool calculation

temperature is below the melting temperature $T_{\text{melting}} = 1733$ K and else it follows

$$\nu = 10^{\left(-0.622 + \frac{2478[K]}{T}\right)} \cdot 10^{-3} \text{ Pa s} \qquad (1)$$

The electrical conductivity, the thermal conductivity, and the specific heat are plotted in Figs. 4, 5, and 6 and are the same as they were used in a previous model [15].

The boundary conditions at the inlet (**a**) and outlet (**c**) are welding velocity v_{welding} and zero electrical potential. The boundary on the weld is a symmetry boundary condition (**b**) and the boundary far away (**d**) is a no-slip wall moving at v-welding with a heat transfer coefficient, which is a combination of the Stefan-Boltzmann approach for radiation and the Newton-Richman heat exchange coefficient [15]

$$\text{HTC} = \frac{1}{2} \cdot 5.67 \cdot 10^{-8} \text{ Wm}^{-2} \text{ K}^{-4} \cdot (T + T_0)$$
$$\cdot \left(T^2 + T_0^2\right) + 20 \text{ Wm}^{-2} \text{ K}^{-1} \qquad (2)$$

and zero potential, where T is the temperature, and $T_0 = 300$ K is the ambient temperature. The bottom boundary is also a no-slip wall, with the same heat transfer coefficient but with ground potential.

The top boundary is again modeled as a no-slip wall with v_{welding}; however, it includes an electrical current density as determined by the dependency in Fig. 2, but only within a specified radius of the heat source R_{HS} around the position where the wire is assumed (x_0, y_0), which is marked with an orange sphere in Fig. 3. In the same area, also a heat flux by the cathode layer is applied, according to Fig. 1. For the case where two areas with different plasma temperatures are considered for the attachment, an inner area with $R_{\text{HS, inner}}$ with the model assuming a plasma temperature of 9000 K and a
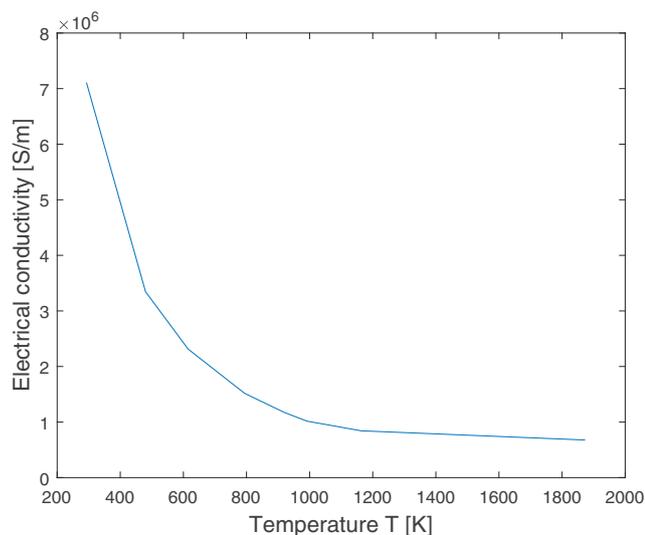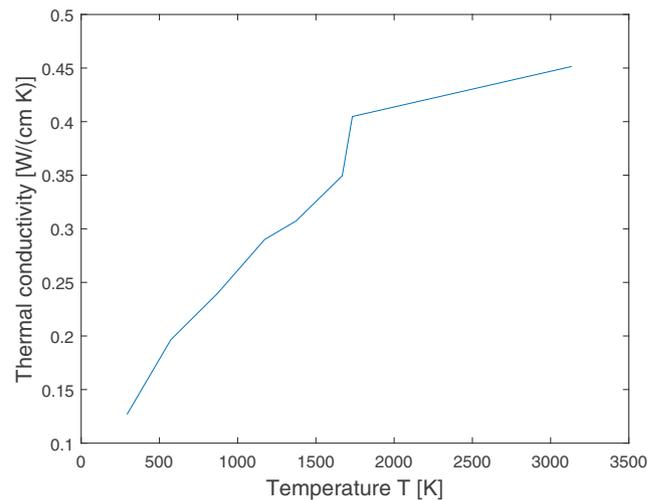
surrounding outer area with the plasma temperature being 13,000 K, which is consistent with the findings about the special structure of the GMAW arc in e.g., [13]. The values in parenthesis in Table 1 denote the values within the inner radius $R_{\text{HS, inner}}$.

Also, a continuous mass source is included, $\dot{m} = 0.0005$ kg s^{-1}, which is distributed within a droplet radius of $R_{\text{Drop}} = 0.5$ mm. The temperature of the mass source was $T_{\text{Drop}} = 2300$ K, and a wire speed which is typical for a given current was taken as the velocity v_{Drop}, as a steady state simulation was performed and the effect of the droplet was considered averaged over time, as discussed in [15]. It should be emphasized that the mass source is not acting periodically as droplets but as a continuous stream.

Over the whole top surface heat losses by evaporation are considered using the model of Knight [6].

For comparison with the Rykalin-Rosenthal heat source [2] Z, the resulting total cathodic power P and total current I were
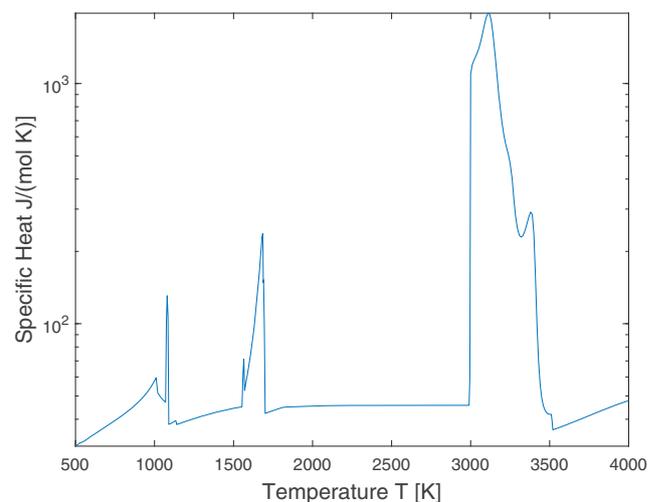

Fig. 5 Thermal conductivity of steel S235JR as used in [15]

Fig. 4 Electrical conductivity of steel S235JR as used in [15]

Fig. 6 Specific heat of steel S235JR as used in [15]

Table 1 Parameters for the simulation (values in parenthesis are valid for the area within the inner radius $R_{HS,\,inner}$)

Figures 7, 8, and 9 (all left)	$T_{\text{Plasma}} = 9000$ K; $U_D = 20$ V; $R_{\text{HS}} = 3$ mm; $v_{\text{weld}} = 30$ cm/min; $R_{\text{Drop}} = 0.5$ mm; $T_{\text{Drop}} = 2300$ K; $v_{\text{Drop}} = 0.053$ m/s
Figures 7, 8, and 9 (all right)	Gauss : $P = 1584$ W; $I = 85$A $R_{\text{HS}} = 3$ mm; $v_{\text{weld}} = 30$ cm/min; $R_{\text{Drop}} = 0.5$ mm; $T_{\text{Drop}} = 2300$ K; $v_{\text{Drop}} = 0.053$ m/s
Figures 10, 11, and 12 (all left)	$T_{\text{Plasma}} = 9000$ K; $U_D = 20$ V; $R_{\text{HS}} = 3$ mm; $v_{\text{weld}} = 60$ cm/min; $R_{\text{Drop}} = 0.5$ mm; $T_{\text{Drop}} = 2300$ K; $v_{\text{Drop}} = 0.053$ m/s
Figures 10, 11, and 12 (all right)	Gauss : $P = 1499$ W; $I = 73$ A; $R_{\text{HS}} = 3$ mm; $v_{\text{weld}} = 60$ cm/min; $R_{\text{Drop}} = 0.5$ mm; $T_{\text{Drop}} = 2300$ K; $v_{\text{Drop}} = 0.053$ m/s
Figures 13, 14, and 15 (all left)	$T_{\text{Plasma}} = 13000$ K (9000 K); $U_D = 20$ V; $R_{\text{HS}} = 5$ (1) mm; $v_{\text{weld}} = 30$ cm/min; $R_{\text{Drop}} = 0.5$ mm; $T_{\text{Drop}} = 2300$ K; $v_{\text{Drop}} = 0.083$ m/s
Figures 13, 14, and 15 (all right)	Gauss : $P = 4594$ W; $I = 331$ A; $R_{\text{HS}} = 5$ (1) mm; $v_{\text{weld}} = 30$ cm/min; $R_{\text{Drop}} = 0.5$ mm; $T_{\text{Drop}} = 2300$ K; $v_{\text{Drop}} = 0.053$ m/s
Figures 16, 17, and 18 (all left)	$T_{\text{Plasma}} = 13000$ K (9000 K); $U_D = 20$ V; $R_{\text{HS}} = 5$ (1) mm; $v_{\text{weld}} = 60$ cm/min; $R_{\text{Drop}} = 0.5$ mm; $T_{\text{Drop}} = 2300$ K; $v_{\text{Drop}} = 0.083$ m/s
Figures 16, 17, and 18 (all right)	Gauss : $P = 2821$ W; $I = 171$ A; $R_{\text{HS}} = 5$ (1) mm; $v_{\text{weld}} = 60$ cm/min; $R_{\text{Drop}} = 0.5$ mm; $T_{\text{Drop}} = 2300$ K; $v_{\text{Drop}} = 0.053$ m/s
Figure 19	$T_{\text{Plasma}} = 13000$ K (9000 K); $U_D = 20$ V; $R_{\text{HS}} = 5$ (1) mm; $v_{\text{weld}} = 30$ cm/min; NoDrop

first determined for each parameter set and then applied as a Rykalin-Rosenthal distribution around (x_0, y_0) with the radius R_{HS} for heat flux and current density.

4 Results

The results of the simulations are depicted in Figs. 7, 8, 9, 10, 11, 12, 13, 14, 15, 16, 17, 18, and 19. Each simulation is depicted in three views. First a view is shown of the top of the weld pool and the longitudinal cross-section with the depiction of the heat flux distribution, including the melt pool shape and the melt pool velocity vectors. It should be noted that, as can be seen from Figs. 1 and 2, the current density distributions follow closely to the heat flux distributions on the weld pool surface; therefore, the depiction of the current density distribution on the weld pool surface was omitted and the heat flux distribution drawn for reference in the further analysis. Also, the total power and the total current are indicated. The second view gives a view of the transversal cross section, including the current density vector field on the right side of the melting isothermal surface. Here, also the weld pool dimensions are indicated. The third view shows the temperature field on the top of the melt pool and along the longitudinal cross section, with the maximum temperature of the weld pool indicated and white contour lines marking melting temperature and boiling temperature on the weld pool surface.

The simulations were performed first with the EDACC model and for comparison with a Rykalin-Rosenthal distribution for heat flux and current density, taking the resulting power P and total current I from the former. The simulation parameters are shown in Table 1.

In the simulation leading to the Fig. 7 (left), Fig. 8 (left), and Fig. 9 (left), a low plasma temperature of $T_{\text{Plasma}} = 9000$ K was assumed acting over a rather constricted area with $R_{\text{HS}} = 3$ mm, going at a small welding speed $v_{\text{weld}} = 30$ cm/min. The resulting weld pool using the EDACC model is wider but more shallow. However, the maximum temperature is below the boiling temperature T_{boiling}, while the maximum temperature using the Rykalin-Rosenthal heat source (Fig. 9 (right)) is above the boiling temperature, leading to increased heat losses by evaporation and therefore a smaller volume of the weld pool. The heat flux in Fig. 7 is highest at the area where the
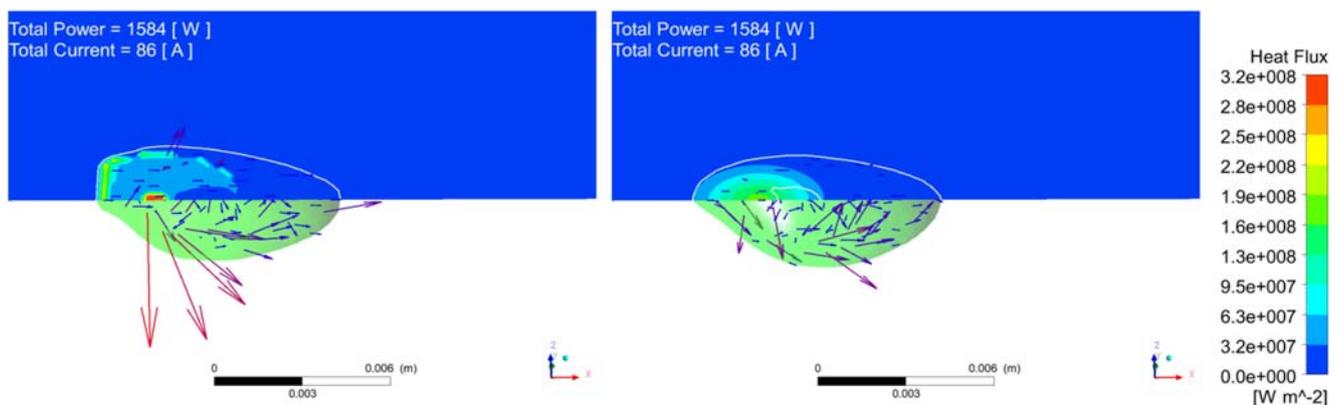

Fig. 7 Heat flux for EDACC model with $T_{\text{plasma}} = 9000$ K; $v_{\text{welding}} = 30$ cm/min (left), Rykalin-Rosenthal model (right)
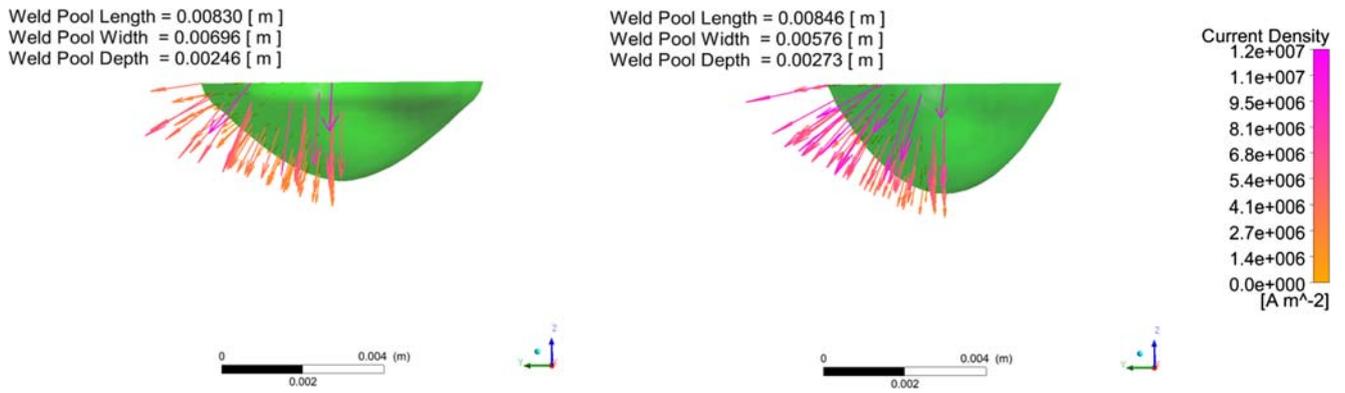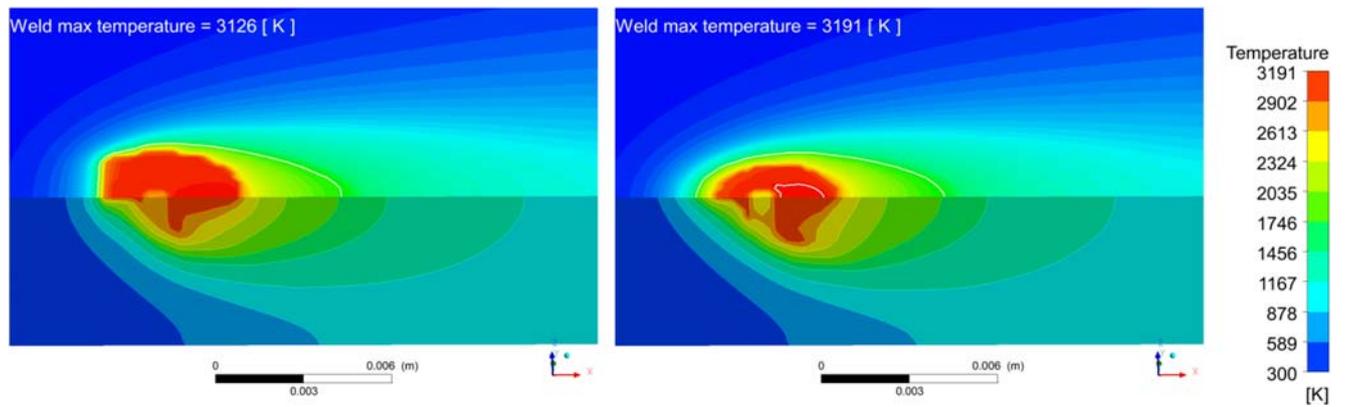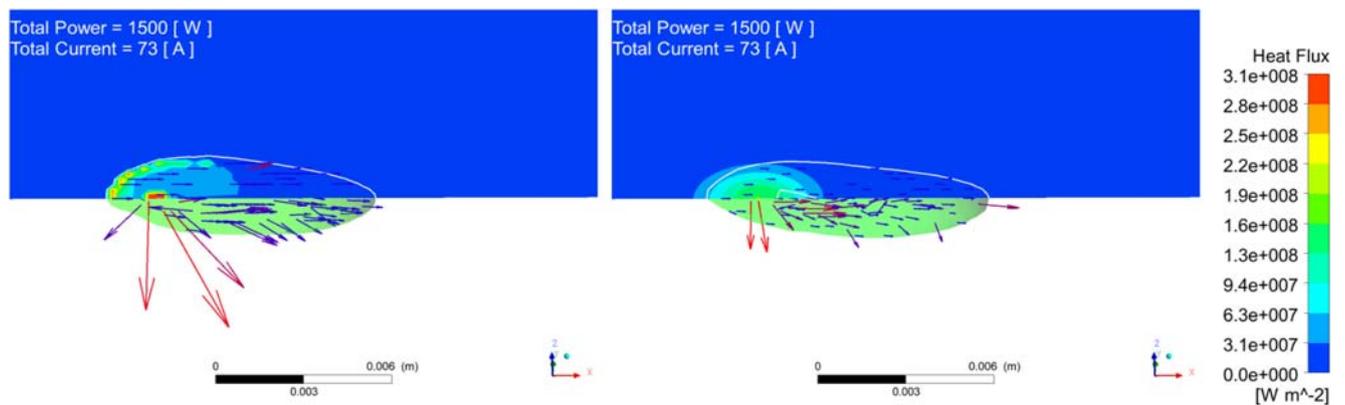
Weld Pool Length = 0.00830 [m]
Weld Pool Width = 0.00696 [m]
Weld Pool Depth = 0.00246 [m]

Weld Pool Length = 0.00846 [m]
Weld Pool Width = 0.00576 [m]
Weld Pool Depth = 0.00273 [m]

Current Density
1.2e+007
1.1e+007
9.5e+006
8.1e+006
6.8e+006
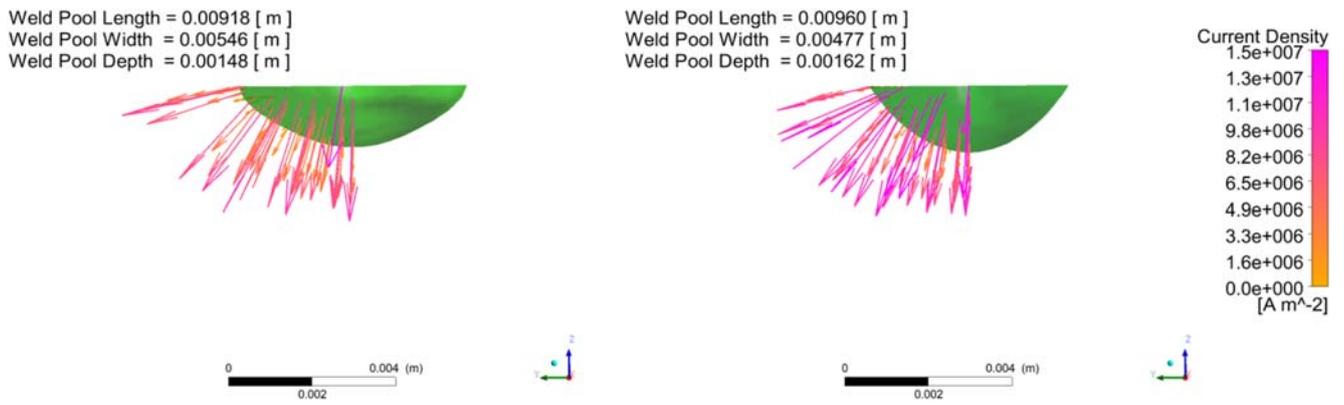5.4e+006
4.1e+006
2.7e+006
1.4e+006
0.0e+000
[A m^-2]

Fig. 8 Cross-section for EDACC model with $T_{plasma} = 9000$ K; $v_{welding} = 30$ cm/min (left), Rykalin-Rosenthal model (right)

Weld max temperature = 3126 [K]

Weld max temperature = 3191 [K]

Temperature
3191
2902
2613
2324
2035
1746
1456
1167
878
589
300
[K]

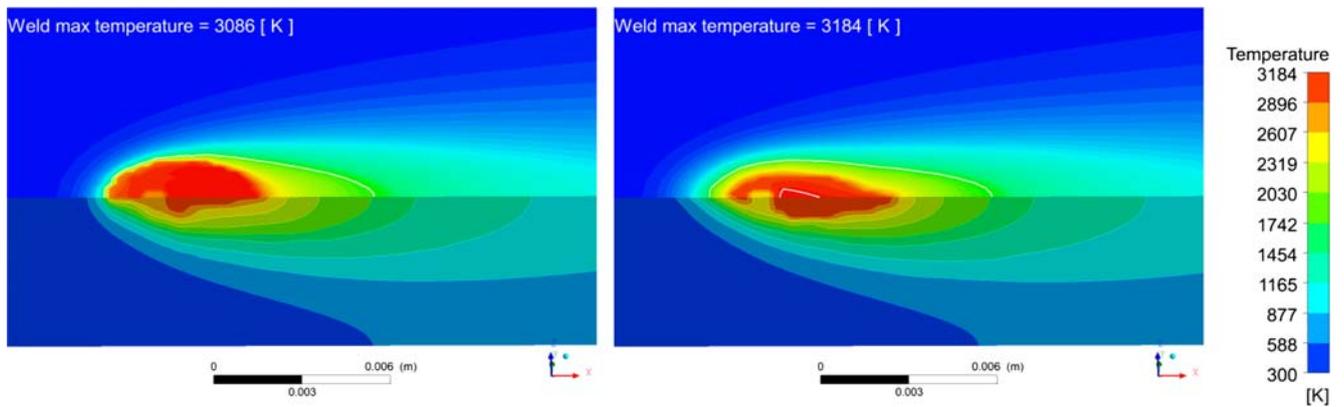**Fig. 9** Temperature for EDACC model with $T_{plasma} = 9000$ K; $v_{welding} = 30$ cm/min (left), Rykalin-Rosenthal model (right)

Total Power = 1500 [W]
Total Current = 73 [A]

Total Power = 1500 [W]
Total Current = 73 [A]

Heat Flux
3.1e+008
2.8e+008
2.5e+008
2.2e+008
1.9e+008
1.6e+008
1.3e+008
9.4e+007
6.3e+007
3.1e+007
0.0e+000
[W m^-2]

Fig. 10 Heat flux for EDACC model with $T_{plasma} = 9000$ K; $v_{welding} = 60$ cm/min(left), Rykalin-Rosenthal model (right)
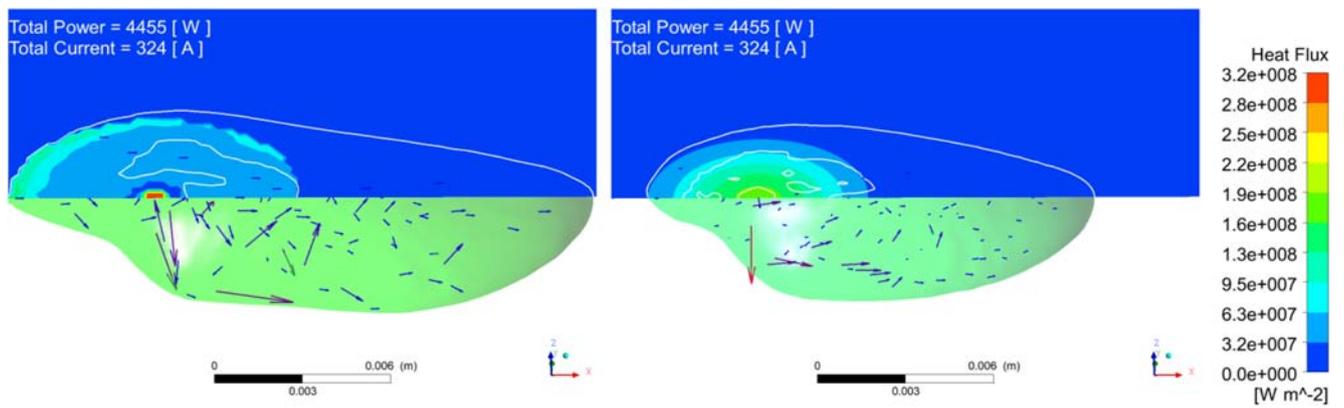
Weld Pool Length = 0.00918 [m]
Weld Pool Width = 0.00546 [m]
Weld Pool Depth = 0.00148 [m]

Weld Pool Length = 0.00960 [m]
Weld Pool Width = 0.00477 [m]
Weld Pool Depth = 0.00162 [m]

Fig. 11 Cross-section for EDACC model with T_{plasma} = 9000 K; $v_{welding}$ = 60 cm/min(left), Rykalin-Rosenthal model (right)

Weld max temperature = 3086 [K]

Weld max temperature = 3184 [K]

Fig. 12 Temperature for EDACC model with T_{plasma} = 9000 K; $v_{welding}$ = 60 cm/min(left), Rykalin-Rosenthal model (right)

Total Power = 4455 [W]
Total Current = 324 [A]

Total Power = 4455 [W]
Total Current = 324 [A]

Fig. 13 Heat flux for EDACC model with $T_{plasma,\ inner}$ = 9000 K; $T_{plasma,\ outter}$ = 13000 K; $v_{welding}$ = 30 cm/min
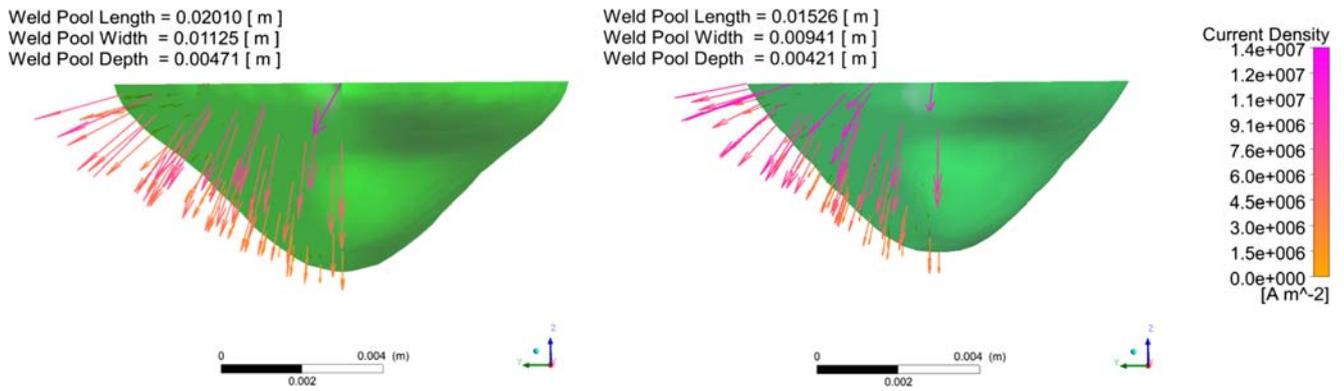
Fig. 14 Cross-section for EDACC model with $T_{plasma, inner} = 9000$ K; $T_{plasma, outter} = 13000$ K; $v_{welding} = 30$ cm/min
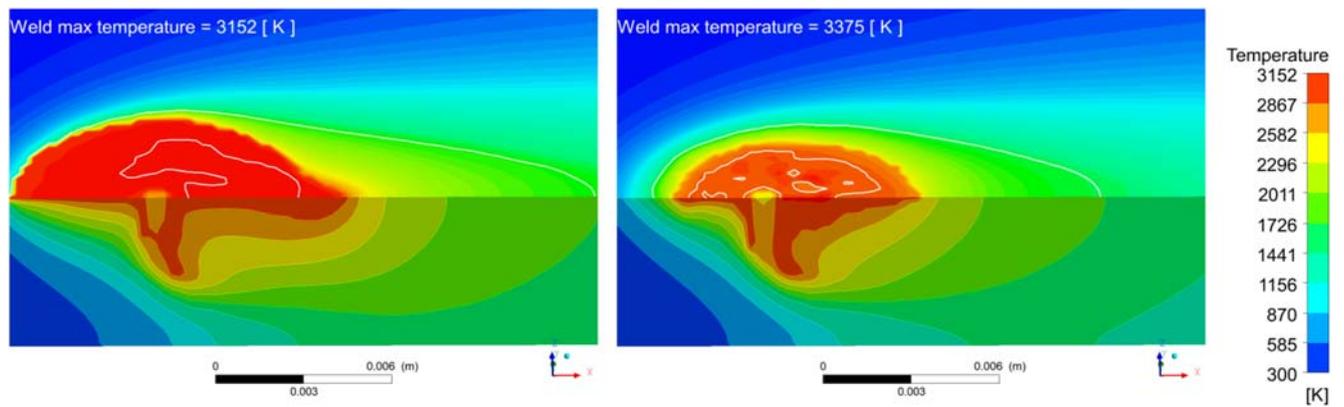
Fig. 15 Temperature for EDACC model with $T_{plasma, inner} = 9000$ K; $T_{plasma, outter} = 13000$ K; $v_{welding} = 30$ cm/min
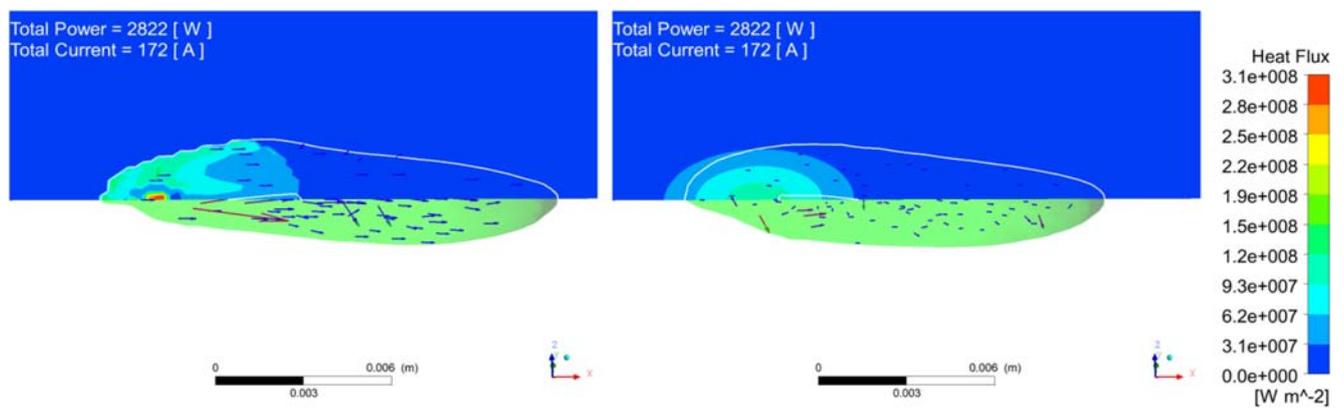
Fig. 16 Heat flux for EDACC model with $T_{plasma, inner} = 9000$ K; $T_{plasma, outter} = 13000$ K; $v_{welding} = 60$ cm/min
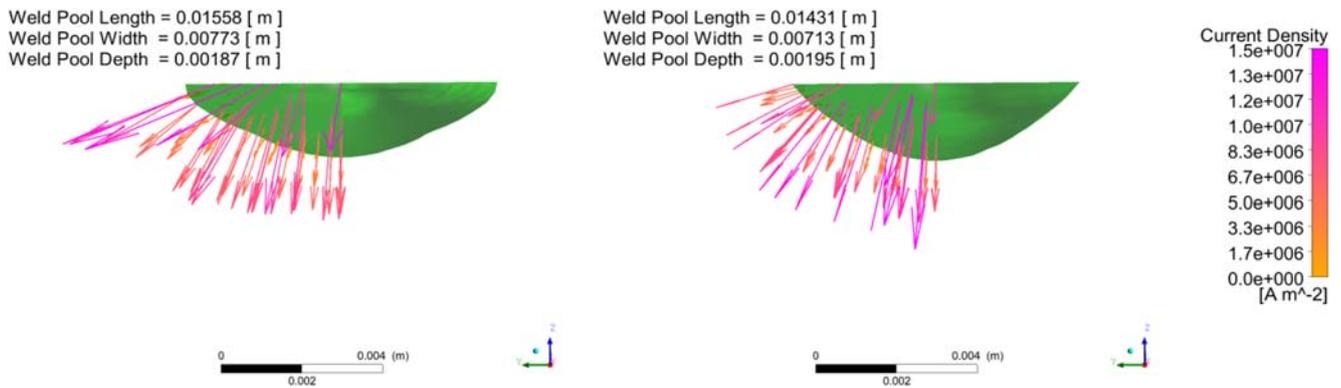
Fig. 17 Cross-section for EDACC model with $T_{plasma,\,inner} = 9000$ K; $T_{plasma,\,outter} = 13000$ K; $v_{welding} = 60$ cm/min

droplets lower the surface temperature, but it also has considerable contributions on the melting front. As the current density follows closely the heat flux distribution, the high concentration of the current density in the area of droplet impingement leads to a strong Lorentz force, increasing the velocity vectors of the melt.

Figures 10, 11, and 12 show the comparison for the same simulation parameters, but with increased welding velocity $v_{weld} = 60$ cm/min. As expected, the weld pools are more shallow than in the case of Figs. 7, 8, and 9. However, the weld pool of the EDACC model is more shallow, while being wider. Again, the maximum temperature in this case is lower than the boiling temperature, while the temperature, in the case with the Rykalin-Rosenthal heat flux and current density, is above (Fig. 12).

The simulations leading to Fig. 13 (left), Fig. 14 (left), and Fig. 15 (left) assumed a heat source where within $R_{HS,\,inner} = 1$ mm the plasma temperature $T_{Plasma} = 9000$ K, while until a radius $R_{HS} = 5$ mm, the plasma temperature was $T_{Plasma} = 13000$ K. The welding velocity was $v_{weld} = 30$ cm/min. In addition, the droplet velocity was adjusted to $v_{Drop} = 0.083$ m/s according to the wire feeding speed. It is seen that most of the heat flux concentrate in the area where the droplets lower the

surface temperature, indicating also a high concentration of the current density and therefore strong Lorentz forces. It should be noted that the maximum temperature of the EDACC model shows only slightly overheating, while the Rykalin-Rosenthal heat source (Fig. 15 (right)) causes an overheating, i.e., a temperature difference above boiling temperature, of more than 200 K, which causes strong evaporation losses and the weld pool dimensions to be considerably smaller.

At higher welding velocities (Figs. 16, 17, and 18), the total power and the total current decrease considerably with the EDACC model, as the area with sufficient temperature for cathodic heating decreased. Also, the concentration of the heat flux (and therefore also of the current density) along the melting front is a slightly higher than in Fig. 13. Overall, the weld pool is more shallow, and the differences between the Rykalin-Rosenthal distribution and the EDACC model are less pronounced.

Lastly, Fig. 19 depicts the situation where the influence of the droplets was switched off. It should be noted that, in this situation, the droplets do not affect the surface temperature. Therefore, a higher concentration of the heat flux and current density has accumulated on the melting front. The maximum temperature is slightly above the boiling temperature.
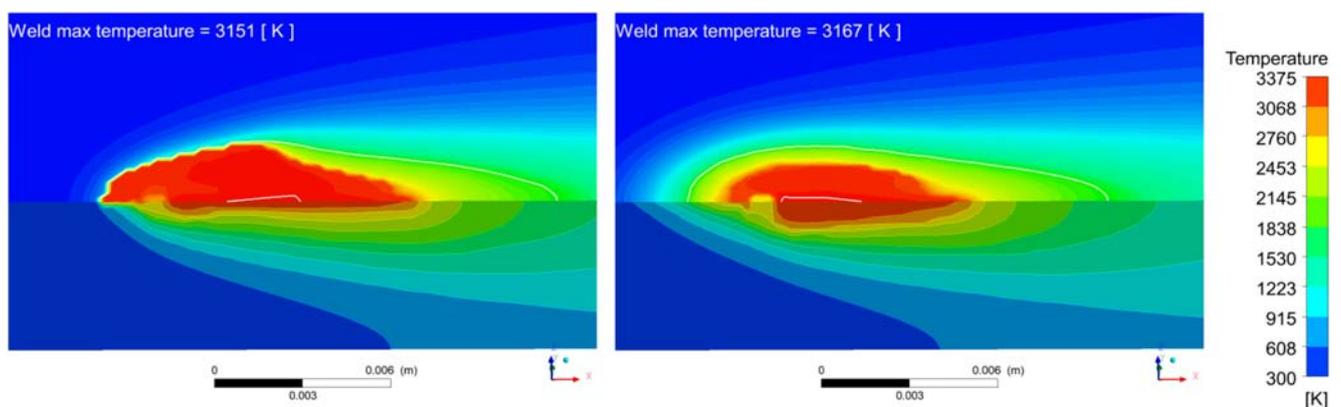

Fig. 18 Temperature for EDACC model with $T_{plasma,\,inner} = 9000$ K; $T_{plasma,\,outter} = 13000$ K; $v_{welding} = 60$ cm/min
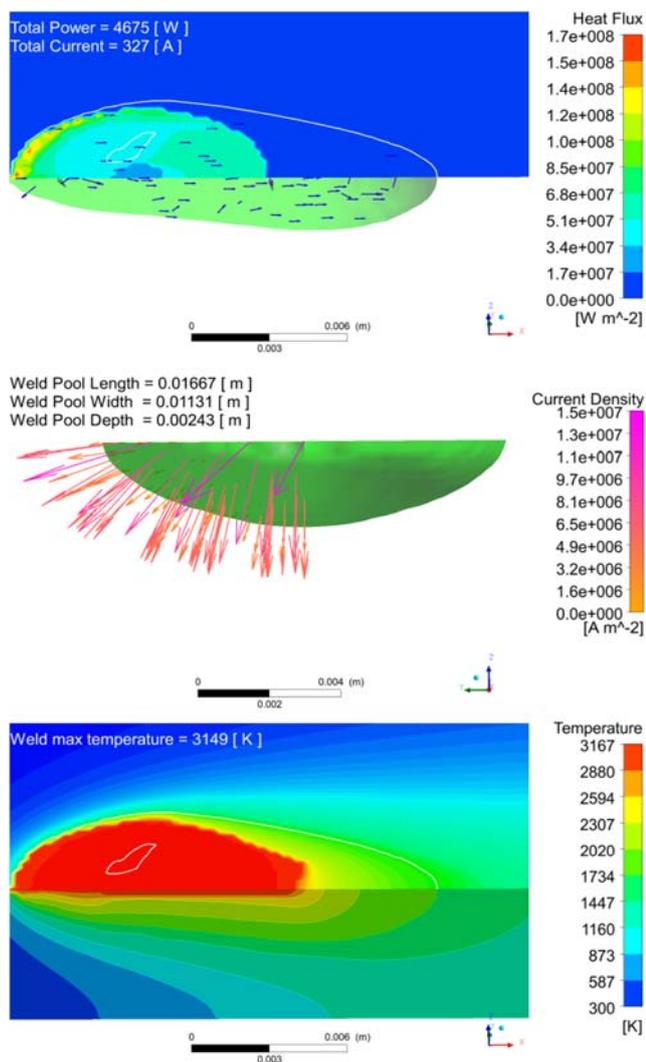
Fig. 19 Heat flux (top), cross-section (center) and Temperature (bottom) for EDACC model with $T_{plasma,\ inner} = 9000$ K; $T_{plasma,\ outter} = 13000$ K; $v_{welding} = 30$ cm/min without droplet influence

5 Discussion

The present work shows qualitatively that the current density and heat flux distribution are highly dependent on the weld pool surface temperature. This temperature is also strongly influenced by the droplets. The arc-cathode attachment therefore changes considerably depending on the droplet temperature, especially if it is hotter than the temperature of maximum heat flux of the EDACC model. Also, in a situation as is for example present in a pulsed process, where the droplet influence is periodical, the shape of the cathode attachment is varied accordingly (compare Fig. 13 with Fig. 19 (top)).

The conditions present in Figs. 13, 14, and 15 show that in the case of the EDACC model, the temperature at the position of the droplet impingement is lower than the weld pool surface temperature outside of that position. This leads to a higher concentration of current density at this position and therefore a stronger Lorentz

force driving the melt downwards to the bottom of the melt pool. So, while the temperature is colder, more heat can be transported downwards (as can be seen from Fig. 14).

The results of the present work also show that the welding speed has an influence on how much heating power can be generated in the cathode layer, by influencing the surface temperature field as can be seen by comparison between Fig. 13 (left) and Fig. 16 (left).

In situations where the weld pool is very shallow, the difference of using either one distribution for heat flux or current density becomes less pronounced, see Figs. 16, 17, and 18, left and right respectively.

Finally, it should be stated that due to the EDACC model, the heat flux interacts with the weld pool surface temperature; the tendency of the Rykalin-Rosenthal approach to overheat the center region of the heat source is strongly avoided, and therefore, also the temperature gradients on the top surface are strongly reduced. The diminishing of the gradients leads to a strong decrease in the Marangoni effect, which is usually assumed as a strong driver for weld pool flows.

Since this study was performed without the consideration of the processes in the GMAW plasma arc column as well as the free surface, the presented results cannot be used to derive quantitative statements.

6 Conclusion

In this work, the effects of a new model for evaporation-determined arc-cathode coupling (EDACC) were investigated. The model determines the heat flux and current density distribution from physical principles and has the main advantage over the currently widely used Rykalin-Rosenthal distribution in that it does not lead to strong overheating of the weld pool surface at the center of the heat source. Another feature is that it is not an axisymmetric distribution in contrast with Rykalin-Rosenthal. The present investigation tries to determine how much the assumption of an axisymmetric heat source influences the results and how far a more realistic model needs to be applied in GMAW process simulation. As axial symmetry can be fairly assumed by the anode, i.e., the wire electrode at the formation of the droplet, but not at the cathode, i.e., the weld pool, the break of symmetry leads to the conclusion that the droplet and the weld pool need to be considered simultaneously to fully account for the complete dynamic of the process. Also, the melt flows are different, and some effects that have been explained by surface tension (like e.g., the Marangoni effect) could be explained by the more accurate modeling of the arc-cathode coupling.

Also, it shows that the areas of maximum heat flux and current density do not coincide with the location of the maximum surface temperature, and therefore, the statements derived from this assumption should be called into question.

Lastly, as an outlook, it is planned to extend the model to allow the consideration of a pulsed process, as well as a free surface.

References

1. Mokrov O et al (2019) Arc-cathode attachment in GMA welding. J Phys D Appl Phys 52:36. https://doi.org/10.1088/1361-6463/ab2bd9
2. Rykalin NN (1957) Berechnung der Wärmevorgänge beim Schweißen (transl.). VEB Verlag Technik, Berlin
3. Jeong H, Park K, Baek S, Kim DY, Kang MJ, Cho J (2018) Three-dimensional numerical analysis of weld pool in GMAW with fillet joint. Int J Precis Eng Manuf 34(8):1171–1177. https://doi.org/10.1007/s12541-018-0138-4
4. Ogino Y, Asai S, Hirata Y (2018) Numerical simulation of WAAM process by a GMAW weld pool model. Welding in the World 62(2): 393–401. https://doi.org/10.1007/s40194-018-0556-z
5. Xu G, Hu J, Tsai HL (2009) Three-dimensional modeling of arc plasma and metal transfer in gas metal arc welding. Int J Heat Mass Transf 52(7):1709–1724. https://doi.org/10.1016/j.ijheatmasstransfer.2008.09.018
6. Knight CJ (1979) Theoretical modelling of rapid surface vaporization with back pressure. AIAA J 17(5):519. https://doi.org/10.2514/3.61164
7. Kozakov R et al (2013) Weld pool temperatures of steel S235 while applying a controlled short-circuit gas metal arc welding process and various shielding gases. J Phys D Appl Phys 46:47. https://doi.org/10.1088/0022-3727/46/47/475501
8. Benilov MS, Marotta A (1995) A model of the cathode region of atmospheric pressure arcs. J Phys D Appl Phys 28(9):1869. https://doi.org/10.1088/0022-3727/28/9/015
9. Benilov MS (1993) Nonlinear heat structures and arc-discharge electrode spots. Phys Rev E 48:506. https://doi.org/10.1103/PhysRevE.48.506
10. Benilov MS (2008) Understanding and modelling plasma–electrode interaction in high-pressure arc discharges: a review. J Phys D Appl Phys 41(14):144001. https://doi.org/10.1088/0022-3727/41/14/144001
11. Zielinska S et al (2007) Investigations of GMAW plasma by optical emission spectroscopy. Plasma Sources Sci Technol 16:832. https://doi.org/10.1088/0963-0252/16/4/019
12. Valensi F et al (2010) Plasma diagnostics in gas metal arc welding by optical emission spectroscopy. J Phys D Appl Phys 43:43400. https://doi.org/10.1088/0022-3727/43/43/434002
13. Kozakov R et al (2013) Spatial structure of the arc in a pulsed GMAW process. J Phys D Appl Phys 46:224001. https://doi.org/10.1088/0022-3727/46/22/224001
14. Rouffet ME et al (2010) Spectroscopic investigation of the high-current phase of a pulsed GMAW process. J Phys D Appl Phys 45(43):189501. https://doi.org/10.1088/0022-3727/43/43/434003
15. Mokrov O et al (2017) Numerical investigation of droplet impact on the welding pool in gas metal arc welding. Mater Sci Eng Technol 48(12):1206–1212. https://doi.org/10.1002/mawe.201700147